Monthly Notices of the ROYAL ASTRONOMICAL SOCIETY

MNRAS **527,** 8931–8940 (2024) https://doi.org/10.1093/mnras/stad3236
Advance Access publication 2023 October 31

Some statistical remarks on GRBs jointly detected by *Fermi* and *Swift* satellites

Sandor Pinter [1,2★] Lajos G. Balazs,[2,3] Zsolt Bagoly,[1,4] L. Viktor Toth [2,5] Istvan I. Racz [1] and Istvan Horvath[1]

[1]*Department of Natural Science, University of Public Service, H-1101 Budapest, Hungary*
[2]*Department of Astronomy, Eötvös University, H-1117 Budapest, Hungary*
[3]*Konkoly Observatory, Research Centre for Astronomy and Earth Sciences, H-1121 Budapest, Hungary*
[4]*Department of Physics of Complex Systems, Eötvös University, H-1117 Budapest, Hungary*
[5]*Faculty of Science and Technology, University of Debrecen, H-4032 Debrecen, Hungary*

Accepted 2023 October 19. Received 2023 October 19; in original form 2023 June 15

ABSTRACT

We made statistical analysis of the *Fermi* GBM and *Swift* BAT observational material, accumulated over 15 yr. We studied how GRB parameters (T_{90} duration, fluence, and peak flux) that were observed by only one satellite differ from those observed by both. In the latter case, it was possible to directly compare the values of the parameters that both satellites measured. The GRBs measured by both satellites were identified using the k-nearest neighbours algorithm in Euclidean distance. In the parameter space we determined the direction in which the jointly detected GRBs differ most from those detected by only one of the instruments using linear discriminant analyses. To get the strength of the relationship between the parameters obtained from the GBM and BAT, a canonical correlation was performed. The GBM and BAT T_{90} distributions were fitted with a linear combination of lognormal functions. The optimal number of such functions required for fit is two for GBM and three for BAT. Contrary to the widely accepted view, we found that the number of lognormal functions required for fitting the observed distribution of GRB durations does not allow us to deduce the number of central engine types responsible for GRBs.

Key words: instrumentation: detectors – methods: statistical – space vehicles: instruments – telescopes – gamma-ray burst: general.

1 INTRODUCTION

GRBs have been known for decades since their discovery by Klebesadel, Strong & Olson (1973). Since then, many ideas and models have been born about their origin attempting to describe the observed data of these events with varying degrees of success (Kumar & Zhang 2015; Zhang 2018). The first measurements of the BATSE instrument on board the *CGRO* satellite (Fishman et al. 1992) have already shown that there are at least two characteristic maxima in the distribution of the bursts' duration data. By the 1990s, researchers divided the GRBs into two categories based on their T_{90} durations: short (≈0.1–1s) and long events (10–100s) (Kouveliotou et al. 1993). The community mostly measure the duration with the T_{90} parameter, which is the duration of the time interval during which 90 per cent of the total observed counts have been detected. In our case, as we see later, these two characteristic peaks are in both *Fermi* and *Swift* T_{90} distributions, although the position of the peaks are different. In the case of short bursts this peak is at 0.6 and 0.25 s, and of long ones at 25s and 40s, for *Fermi* and *Swift* bursts, respectively.

To explain these two peaks, researchers generally agree that the models can be divided into two large groups.

One of them assumes that short duration GRBs are originating from merging two compact objects (neutron star, black hole, or possibly a white dwarf). Analysing GRB light curves one can find those that best fits one of these mechanisms (Rueda et al. 2018b).

GRBs with long (>10s) durations are typically caused by collapsing high mass (>10 $M_\odot$) stars. In some cases, however, merging two compact objects may also produce long GRBs (Rueda et al. 2018a). King, Olsson & Davies (2007) also presented arguments for producing long GRBs by merging a massive white dwarf with a neutron star. Of course, all these models are theoretically possible.

There are also ideas that cannot be fitted to any of the above models. Huang et al. (2003), for example, believe that GRBs may also be formed by a neutron star kick. Bombaci & Datta (2000) studied the conversion of a neutron star to a strange star as a possible energy source for GRBs.

Naturally, all these models can be realized, however, not necessarily with the same frequency in a GRB sample, collected from observations. The two well-defined peaks in the T_{90} distribution may indicate that one of the models is dominant for the short GRBs and another for the long ones. Of course, this is just a statistical argument. In the case of some specific GRBs, it is necessary to carefully analyse whether one of the options has been realized or whether we are facing a new case that has not been studied in theory so far.

The distribution of T_{90}, observed by BATSE, could be approximated by the superposition of two lognormal distributions. However,

★ E-mail: sandor.pinter@uni-nke.hu

Horváth (1998) and Mukherjee et al. (1998) showed that supposing a third, intermediate lognormal group fits the T_{90} distribution much better. Many authors (Hakkila et al. 2000; Balastegui, Ruiz-Lapuente & Canal 2001; Horváth 2002; Borgonovo 2004; Horváth et al. 2004; Chattopadhyay et al. 2007; Zitouni et al. 2015) have since confirmed the existence of this intermediate GRB class in the same data base using different techniques.

Analysing T_{90} distribution obtained by the *Swift* satellite also resulted in the existence of a third, intermediate group between the short and long GRBs (Horváth et al. 2008; Huja, Mészáros & Řípa 2009; Horváth et al. 2010; Zitouni et al. 2015; Horváth & Tóth 2016; Deng et al. 2022). For the *Fermi* GRBs there are also many single or multidimensional analysis, about this topic (Tarnopolski 2015, 2016; Horváth et al. 2019; Tarnopolski 2019; Salmon, Hanlon & Martin-Carrillo 2022; Zhang et al. 2022).

Whether we look at merging or collapsar models, a very compact object is created for both types. This is the fireball model by Meszaros & Rees (1993). The energy condensed in this extremely small volume is released in a very short-lived explosion and creates the GRB phenomenon observed (Piran 2004; Mészáros 2006; Pe'er 2015).

The compact objects created in the models outlined above, in which the compressed energy is released in the form of GRB, differ in the extremely small volume in the compressed energy and in the time-scale of the burst dynamics. The lognormal peak in the T_{90} distribution supports the dominance of any of these.

The question arises, does the third lognormal peak suggest the presence of a third type of central engine for intermediate T_{90} duration GRBs? We may get closer to the answer, if we look at the GRBs that both *Fermi* and *Swift* detected.

1.1 Differences in observations' strategies

The Neil Gehrels Swift Observatory and the *Fermi* Gamma-ray Space Telescope have different technical layout and observational strategy. *Swift* has three major observational facilities: a coded mask for gamma-ray detection (Burst Alert Telescope, BAT), and two telescopes for X-ray and Ultra-Violet/Optical range (XRT and UVOT, respectively) (Gehrels et al. 2004; Barthelmy et al. 2005).

The *Swift* is operating in observatory mode, which means, after getting a burst alert, the BAT is slewing to point to the burst's direction in the sky (Barthelmy et al. 2000, 2005). BAT covers a large fraction of the sky (over one steradian fully coded, three steradians partially coded; by comparison, the full sky solid angle is 4π or about 12.6 steradians). It locates the position of each event with an accuracy of 1 to 4 arcmin within 15 s. The BAT is sensitive in the 15–150 keV energy range.

The XRT can take images and perform spectral analysis of the GRB afterglow. This provides more precise location of the GRB, with a typical error circle of approximately 2 arcsec radius. The XRT is also used to perform long-term monitoring of GRB afterglow light curves for days to weeks after the event, depending on the brightness of the afterglow (Wells et al. 1992; Citterio et al. 1996; Holland et al. 1996; Wells et al. 1997; Short, Keay & Turner 1998; Burrows et al. 2000; Hill et al. 2000). The XRT is sensitive in the 0.2–10 keV energy range. The UVOT is used to detect optical afterglows. The UVOT provides a subarcsecond position and makes optical and ultraviolet photometry (Fordham et al. 1989; Mason et al. 2001; Roming et al. 2005). We note that we used the refined position data gathered by XRT and UVOT instruments (where available) in this study, as they are much more accurate than those from the BAT instrument.

The *Swift* strategy is to reach all new GRB positions as soon as possible and follow all the GRB afterglows as long as the signal can be distinguished from the background noise of the detector. The rotation time of the *Swift* baseline is less than about 90 s. XRT and UVOT observations begin while the burst is still in progress. When *Swift* is blocked in pointing to prompt observations of the most recent bursts, it will follow a schedule uploaded from the ground. This schedule makes possible to follow-up the GRB afterglows when they are in the line of sight of the detectors as long as possible, until the observable brightness of the burst become fainter than the sensitivity threshold of the detectors.

Fermi includes two scientific instruments, the Large Area Telescope (LAT) and the Gamma-ray Burst Monitor (GBM) (Goldstein et al. 2012; Paciesas et al. 2012; Gruber et al. 2014; von Kienlin et al. 2014; Narayana Bhat et al. 2016; von Kienlin et al. 2020). The energy range of the LAT detector is from 20 MeV to 300 GeV, this instrument detects at much higher energies than the *Swift* BAT (Atwood et al. 2009).

The GBM consists of 14 scintillation detectors (twelve sodium iodide crystals for the 8 keV to 1 MeV range and two bismuth germanate crystals with sensitivity from 150 keV to 30 MeV), and can detect gamma-ray bursts in that energy range across the whole 4π area of the sky not occluded by the Earth (Bhat et al. 2009; Bissaldi et al. 2009).

For the first few years of the *Fermi* mission the default observation mode was an all sky survey, optimized to provide relatively uniform coverage of the entire sky with the LAT instrument every three hours. More than 95 per cent of the missions were carried out in this observation mode. However, *Fermi*'s flexible survey mode is capable of patterns and inertially pointed observations, all of which allow for increased coverage of selected parts of the sky.

Due to the different energy response characteristics, technical layout, and observational strategy, the GRBs detected by *Swift* is not necessarily detected by *Fermi* and vice versa. It is an important problem, therefore, to study which part of the GRB population is observed by both of the satellites and which one is observed only by one of them. Furthermore, it is also important to know if there are physical differences between these classes (Racz et al. 2018a, b).

To compare the physical parameters of the GRB detected by BAT and GBM, we used the physical quantities obtained from measurements of both satellites. These parameters are the following: duration (T_{90}), fluence, and 1024 ms peak flux.

1.2 Comparison of BAT and GBM GRB triggering

The BAT burst trigger algorithm looks for count rates over the estimated background and constant sources. The algorithm is constantly examining the criteria that determine the pre-burst background. The BAT processor continuously follows hundreds of such criteria in the same time. The burst trigger threshold is adjustable by program between 4 and 11 sigma above background noise, typically 8 sigma value. One of the most important features of BAT is its imaging ability.

After the burst triggers, the onboard software checks that the trigger comes from a point source, thus many background sources can be eliminated. This yields a GRB fluence sensitivity of $\approx 10^{-8}\,\mathrm{erg\,cm^{-2}\,s^{-1}}$ (in 15–150 keV range), corresponding to $\approx 0.1\,\mathrm{cm^{-2}\,s^{-1}}$ at 75 keV, the middle of the energy range of BAT sensitivity.

A GBM burst trigger occurs when the onboard software detects an increase in the count rate of two or more NaI detectors above an adjustable threshold in units of background count rate standard

deviation (4.5–7.5σ). The trigger algorithms uses four BATSE compatible energy ranges (25–50, 50–300, 100–300, and >300 keV) and ten different time-scales between 16 ms and 8.192s. There are 120 distinct trigger algorithms available, with approximately 75 of them typically operating concurrently. *Fermi* GBM's burst sensitivity (the peak 50–300 keV flux for 5σ detection) is less than 0.5 ph cm^{-2} s^{-1}.

Since the background estimation is different for the two satellites the integrated T_{90} calculations are using different methods. The BAT's coded mask restoration algorithm inherently includes the background subtraction, leaving only the statistical fluctuation in the light-curve data. In the GBM case the values of the T_{90} from a light curve relies on the background estimation. To estimate the background during a GBM trigger, a common technique is to select background intervals on either side of the trigger and interpolate using a polynomial function. Another approach involves acquiring background spectra from orbits on preceding and subsequent days when the spacecraft occupied a similar geomagnetic position in its orbit (Fitzpatrick et al. 2012). For the precise background determination one could also take the detailed positional information of the satellite and the celestial objects (Earth, Sun, and Moon) into account (Szécsi et al. 2013), or use a physically motivated detailed background model for the GBM (Biltzinger et al. 2020). Other information maximalization techniques can also be used, e.g. the Automatized Detector Weight Optimization which maximizes the signal's peak over the background's peak over the search interval (Bagoly et al. 2016).

Although, the energy sensitivity range of GBM is much wider than that of BAT, the higher sensitivity of BAT might result in triggering GRBs in BAT but not in GBM. It can happen that only one of BAT or GBM is triggered, but if it is the case at both satellites, the observed physical parameters of GRBs will be different due to the different spectral characteristics of BAT and GBM.

2 DATA AND METHODS

Our main data base consists all GRBs of *Swift*[1] and *Fermi*[2] detections from the beginning of their missions (2004 December 17 for *Swift* and 2008 July 14 for *Fermi*) until 2023 April 14. We used only those GRBs in our analysis when both satellites were observing simultaneously: from the first observation of *Fermi*.

First we assigned an angular position–trigger time frame to the GRBs detected by the *Swift* and *Fermi* satellites, respectively. For the detailed procedure see Racz et al. (2018a, b). Then we identified the closest Fermi-Swift pairs in this coordinate frame using the *knn* procedure in the *FNN* library of the **R** statistical program (R Core Team 2017; Beygelzimer et al. 2019). The k-nearest neighbours algorithm (knn) is a non-parametric statistical method where the classification is decided by majority vote, with ties broken at random, for each row of the test set's k nearest (in Euclidean distance) training set vectors (k is a positive integer, typically small) (Ripley 1996; Venables & Ripley 2002). If $k = 1$, then the object is simply assigned to the class of that single nearest neighbour as was in our study. The results can be seen in Fig. 1.

[1] *Swift* BAT: https://swift.gsfc.nasa.gov/archive/grb_table/
[2] *Fermi* GBM: https://heasarc.gsfc.nasa.gov/W3Browse/fermi/fermigbrst.html

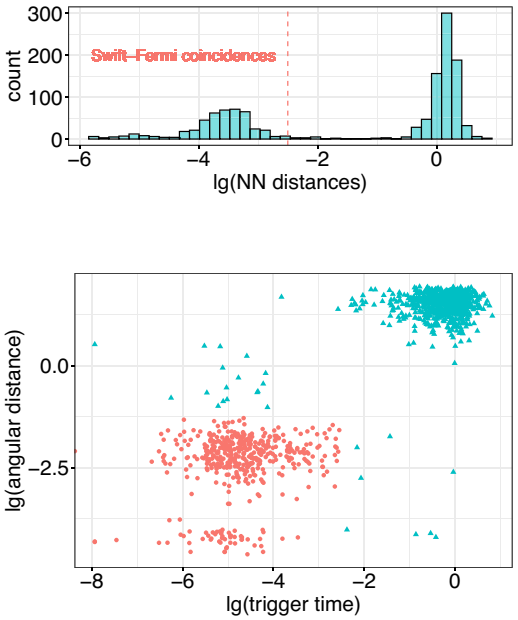

Figure 1. *Upper panel* shows frequency distribution of Euclidean nearest neighbour distances between *Fermi* and *Swift* GRBs, in angular position–trigger time parameter space. Red dashed line marks the boundary between real and random coincidences. *Lower panel* shows the distribution of nearest neighbour GRBs in the angular position (measured in degrees) trigger time (measured in days) difference plane. Light red circles indicate real coincidences. The small lower bump in the left of the image represent GRBs not having durations estimated independently in BAT and GBM data.

2.1 Comparing the physical properties of 'couples' and 'widows' GRBs in BAT and GBM

We have already mentioned in the introduction that the technical layout of the *Swift* and *Fermi* satellites and, consequently, their observational strategies are different. So the question arises on which it depends whether a burst is detected by both satellites, and when only one of them. It may be a simple geometric effect, i.e. the corresponding burst is not in the observed region of the sky at one of the satellites.

In that case if the burst is in the field of view of both satellites but below the detection limit of one of them, the statistical distribution of the physical parameters of the bursts could be different. Namely, in case of a simple geometric selection effect the statistics of the physical properties of both the 'couples' (GRBs detected by both satellites) and 'widows' (observed by only one satellite) bursts should be the same. In the second case, however, when the successful observation depends on the detection limit of the instrument it is not necessarily true.

Motivated by these facts it is worth comparing the statistical properties of 'widows' and 'couples' GRBs detected by both or only one of the satellites. In the following we discuss these issues in case of *Swift* BAT and *Fermi* GBM, separately.

2.2 Creating 'couples' and 'widows' frames

The results of computing k nearest neighbour distances enabled us to create three data frames: Swift–Fermi 'couples', Swift 'widows', and Fermi 'widows'. These names refer to GRBs detected by both *Swift* and *Fermi* satellites, or detected only by *Swift* or only by *Fermi*, respectively.

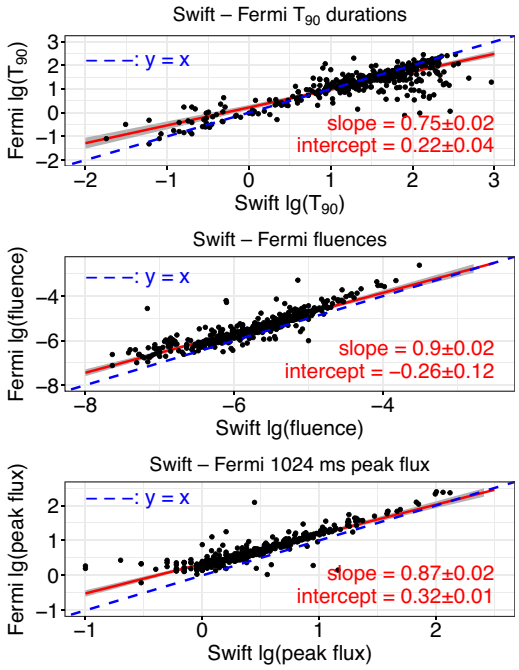

Figure 2. Comparison of T_{90} [s] duration (top), fluence [erg cm^{-2}] (middle), and peak flux [count cm^{-2} s^{-1}] (bottom) of *Fermi* and *Swift*.The X coordinate corresponds to the *Swift* and the Y to the *Fermi* data. At the medium T_{90} the values obtained from the measurements of the two satellites are almost the same, while at the shorter and longer T_{90} duration the values of *Fermi* are systematically higher and lower, respectively. For fluence and peak flux the values obtained from *Fermi* measurements are systematically higher. The dashed blue line indicates the same identical values obtained by the two satellites. The solid red lines are fitted linear regressions with a 5σ confidence error envelope of the fit in grey.

Of course, only the time interval in which both *Swift* and *Fermi* were operating simultaneously should be taken into account in identifying the 'widows'. In identifying the 'couples' this condition is fulfilled automatically. For the differences between the basic parameters of 'couples' group observed by the different satellites (see Fig. 2).

To compare the GRBs detected by the *Swift* and *Fermi* satellites, we used T_{90} duration, fluence, and peak flux physical parameters derived from the measurements of both satellites.[3] The parameters were determined from photons incoming in the 15–150 keV energy range for the *Swift* (Gehrels et al. 2004) and 10–1000 keV for the *Fermi* (Meegan et al. 2009).

Fig. 2 shows even at first glance that the relationship between the quantities measured by BAT and GBM cannot be characterized simply by the $y = x$ line. For duration, the slope is different, while for fluence and peak flux, the values measured by *Fermi* are systematically higher. These differences can be explained by the fact that the energy range of GBM includes the energy range of BAT, however, GBM also detects photons with much higher energy.

In the following, we study the differences in the values of the physical variables characterizing the 'couples' and 'widows' GRBs detected by BAT and GBM. The linear discriminant method was used for this purpose.

[3]For definitions of these parameters, see footnotes 1 and 2.

We also study how the GRBs detected by both satellites differ in the observed variables. For this purpose, the canonical correlation was used. In both procedures, the linear (Pearson) correlation plays an important role. This type of correlation is sensitive to outliers in the data. A usual way using logarithmic variables to suppress their effect in the analysis. We proceeded in this way in our computations.

2.3 Linear discriminant analysis basics

Linear discriminant analysis (LDA) is a method used in statistics to find a linear combination of features that characterizes or separates two or more classes of objects or events.

This method allows us to consider a collection of p measured variables on n cases that are classified into one of the given k classes (here $k = 2$). We look for linear combination of the $\{x_1, x_2,..., x_p\}$ variables which give maximal separation between the groups of the cases. It means we are looking for the variable

$$y = n_1x_1 + n_2x_2 + ... + n_px_p \quad \text{where} \quad n_1^2 + n_2^2 + ... + n_p^2 = 1, \tag{1}$$

with a suitable chosen $\{n_1, n_2,..., n_p\}$ coefficients ensuring a maximal separation between the classes.

2.4 LDA of 'couples' and 'widows' in BAT and GBM data

To get the best performing direction we performed LDA in the parameter space (Fischer 1936; Martinez & Kak 2001; Yu & Yang 2001; McLachlan 2004). LDA is available in the *MASS* library of the **R** project (Venables & Ripley 2002; Racz et al. 2018b). Performing LDA on BAT data we got a very pronounced difference between the 'couples' and 'widows' GRBs detected by the *Swift* satellite.

Similarly to the analysis of *Swift* BAT data we can look for the most discriminating direction between the 'couples' and 'widows' in the parameter space of the observed *Fermi* GBM data. The difference between GBM's 'couples' and 'widows' is much less pronounced than the difference between *Swift*'s 'couples' and 'widows'.

The results will be discussed in detail in Section 3.1.

2.5 Canonical correlation basics

Canonical Correlation analysis (CC) is a statistical method to reveal correlations between two data sets (Hotelling 1933). The canonical correlation analysis is able to identify relationships between linear combinations of the first data set's (X) variables and the linear combinations of the second's (Y).

The canonical correlation assumes we have two set of variables: X and Y. The first set, X, contains $\{x_1, x_2,..., x_m\}$ and Y, the second one, $\{y_1, y_2,..., y_r\}$ variables. We make n observations for each variables. Using the linear combination of the X and Y variables we develop

$$U = (a_1)(x_1) + (a_2)(x_2) + ... + (a_m)(x_m), \tag{2}$$

and

$$V = (b_1)(y_1) + (b_2)(y_2) + ... + (b_r)(y_r), \tag{3}$$

asking: how can one select the 'a' and 'b' set of coefficients so that correlation between U and V, obtained above, has the maximum value.

However, the direction thus obtained does not necessarily characterize all relationships between X and Y variables. All directions perpendicular to directions $\boldsymbol{a}$ and $\boldsymbol{b}$ form a subspace in the parameter space of X and Y, respectively, in which we can find another ($\boldsymbol{a}$, $\boldsymbol{b}$) pair,

which denotes the directions along which the correlation between U and V is maximal. Repeating this procedure, we get the variables ($U1$, $U2$,..., Up) and ($V1$, $V2$,..., Vp) (p is the smaller of m and r) in the X and Y spaces, respectively. The components of their $\boldsymbol{a}$ and $\boldsymbol{b}$ vectors indicate the input variables.

For performing canonical correlations we used the *cc()* procedure in *CCA* library of the **R** statistical package (González & Déjean 2021). However, the correlation between the U and V variables thus obtained is not necessarily significant.

We tested the significance of the variables obtained applying Wilks' λ-test implemented in *p.asym()* procedure in *CCP* library of **R** (Menzel 2012).

For performing the test the Wilk's Λ variable is defined as

$$\Lambda = \prod_{i=1}^{p}(1-\lambda_i), \tag{4}$$

where λ_i are the squared correlations between U_i and V_i vectors.

Having n independent observations the following equation defines a χ^2 distribution of $m \times r$ degrees of freedom:

$$\chi^2 = -[n-1-0.5(m+r+1)]\ln(\Lambda). \tag{5}$$

We set up the null hypothesis that X and Y set of variables are uncorrelated. If we reject this hypothesis (assuming significant correlation) then we remove the first (maximal) λ from equation (4) getting a further χ^2 variable with $(m-1)\times(r-1)$ degrees of freedom, and repeat the test of significance. Only those pairs of canonical variables are interpreted which have passed the test of significance.

2.6 Canonical correlations between BAT and GBM 'couples' data

In our case we have *Swift* (denoted with X) and *Fermi* (denoted with Y) data for the same GRBs, observed by both satellite. In this case $m = r = 3$ (here the observed parameters are the duration, the fluence, and the peak flux). The BAT and GBM data from the two set of variables represent the input of the canonical correlation.

Maximizing the correlation between the U and V variables yields a unit vector (a_1, a_2, a_3) in the parameter spaces of the BAT variables and (b_1, b_2, b_3) in the parameter space of those in GBM. The vectors $\boldsymbol{a}$ and $\boldsymbol{b}$ denote the direction in the space of the BAT and GBM variables along which the correlation between the U and V is maximal. The components of the vectors $\boldsymbol{a}$ and $\boldsymbol{b}$, respectively, indicate how strongly the variables of BAT and GBM participate in this correlation.

3 DISCUSSION

3.1 Remarks to LDA on *Swift* BAT and *Fermi* GBM data

The discriminant analysis between *Swift* 'couples' and 'widows' revealed that the joint distribution of the *Swift* 'couples' and 'widows' T_{90}, fluence and peak flux variables differ at a very high level of significance (Fig. 3). The LD1 variable describing the highest discrimination between *Swift* 'couples' and 'widows' has the highest correlation with fluence followed by peak flux then by T_{90}. The highest contribution, correlation to the LD1 discriminant variable is given in absolute value by the fluence (0.69), followed by the peak flux (0.52), and the T_{90} duration at the end (0.51). (The difference between the mean values in 'couples' and 'widows' groups is given in Table 1.) The H_0 hypothesis assumes that the two samples are the same. We found that the probability of this (the significance p-value)

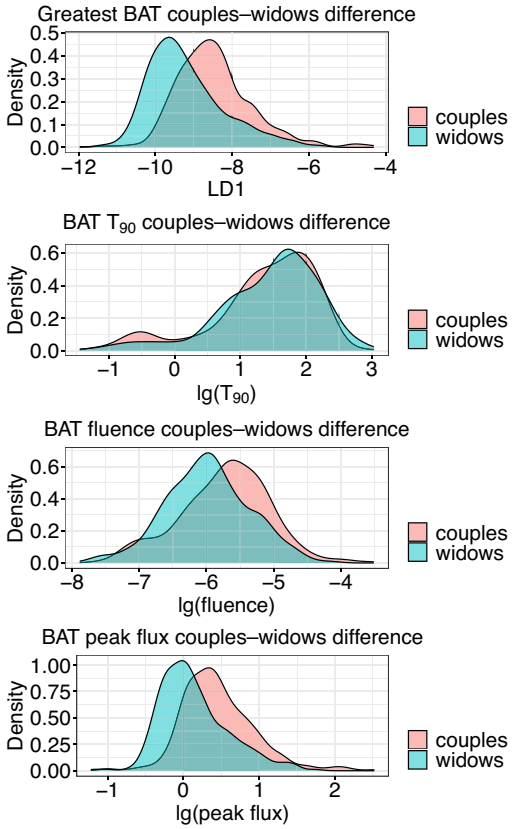

Figure 3. Separation of *Swift* BAT 'couples' and 'widows' GRBs along the best discriminating direction (LD1) obtained by the LDA (upper panel), and the degree of differences of each measured variable. Apparently, the highest difference in measured variables is given by the peak flux. See the text for the definition of the LD1 dimension-less variable.

Table 1. Differences between 'couples' and 'widows' groups in BAT LDA. The error probability for rejecting the null hypothesis, i.e. differing the groups only by chance, is less than 2×10^{-16}.

	Group	LD1	$\log_{10}(T_{90})$	$\log_{10}$(Flu)	$\log_{10}$(Peak)
1	Couples	8.45	1.35	−5.73	0.46
2	Widows	9.20	1.43	−5.98	0.14

is $<2 \times 10^{-16}$, thus we need to reject the H_0 hypothesis, i.e. the two distributions are different.

The mean values of these variables are higher in the 'couples' than in the 'widows' group. The means of T_{90} duration are higher in the 'widows' group. The smaller mean value of T_{90} is caused by a slight surplus of short GRBs in the 'couples' group.

An interesting result of the LDA is an apparent deficit of intermediate duration GRBs in the T_{90} distribution at 'couples', and in the contrary, the short duration GRBs are somewhat fewer at the 'widows' (Fig. 3).

These results are consistent with that obtained by Burns et al. (2016) finding that BAT detects weaker short duration GRBs than GBM.

In the case of BAT, the largest difference between 'couples' and 'widows' is in fluence, but there are also significant differences in peak flux and T_{90} values.

Apparently, the distribution of the Fermi GBM 'couples' and 'widows' variables (Table 2, Fig. 4) differs much less from that

Table 2. Differences between 'couples' and 'widows' groups in GBM LDA. The probability for differing the group only by chance is 3.23×10^{-5}. It is still significant, but much less pronounced than *Swift* BAT.

	Group	LD1	$\log_{10}(T_{90})$	$\log_{10}$(Flu)	$\log_{10}$(Peak)
1	Couples	2.86	1.22	−5.43	0.72
2	Widows	3.07	1.10	−5.57	0.64

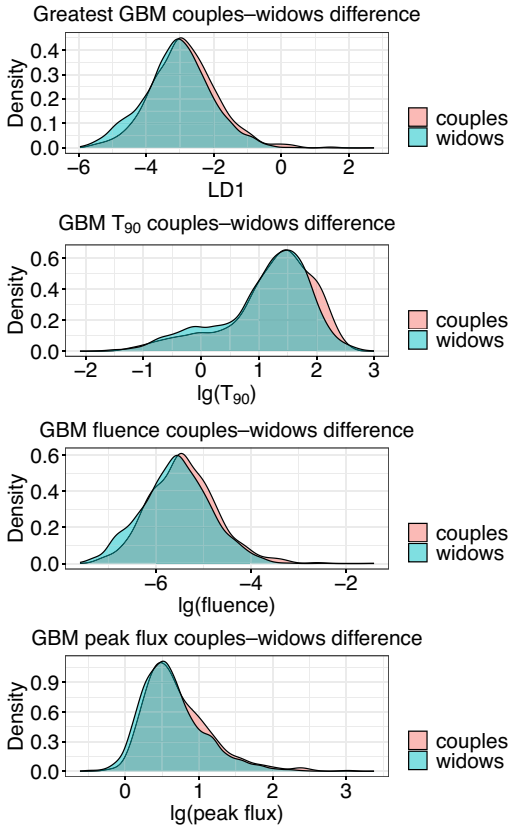

Figure 4. Separation of *Fermi* GBM 'couples' and 'widows' GRBs along the best discriminating direction (LD1) obtained by the LDA (upper panel) and the degree of contribution of each measured variable. The units of variables are as before. Apparently, the difference between 'couples' and 'widows' is much less pronounced than in BAT. The greatest contribution to the 'couples' 'widows' difference is given by the fluence.

of the *Swift* BAT (the significance p-value is 3.23×10^{-5}). This phenomenon may be partly explained by the fact that the *Swift* sees a much smaller part of the sky compared to the *Fermi*. So at some given event, there could be also GRBs among the *Fermi* 'widows' category that would belong to the 'couples' group if they fell into *Swift*'s field of view.

In case of GBM, the most significant difference appears in the distribution of peak fluxes and fluences. The highest contribution, correlation to the LD1 discriminant variable is given in absolute value by the peak flux (0.75), followed by the fluence (0.61) and the T_{90} (0.27) at the end.

The duration of the 'couples' bursts appears to be significantly longer. As the longer duration bursts are softer, a higher percentage of incoming photons fall within the range of energy detected by BAT. The 'couples' bursts' fluence is also larger than the 'widows' due to the correlation with duration.

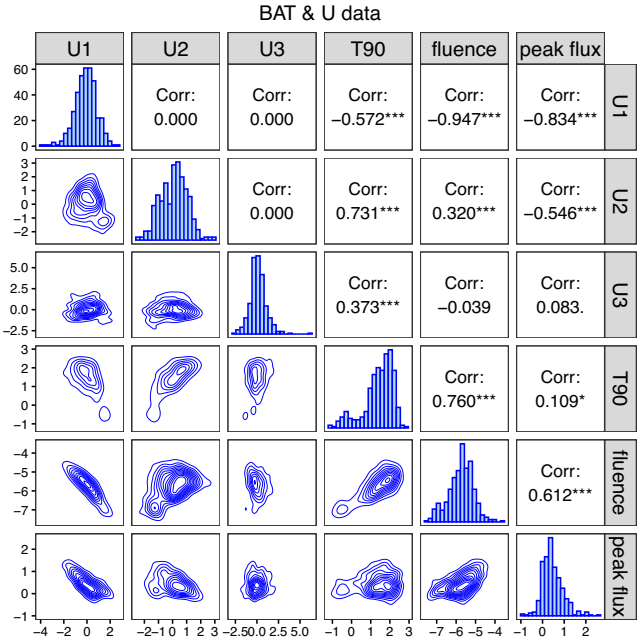

Figure 5. Matrix plot of BAT data and the canonical variables obtained from BAT (*U1,U2,U3*). Lower triangle panels show 2D densities the upper triangle ones the correlations between the variables. The significance level of the correlation indicated with stars at the right side of the numbers. Seemingly, the first (the strongest) canonical variable (*U1*) has the tightest correlation with fluence.

3.2 Remarks to canonical correlation between BAT and GBM 'couples'

Using the canonical variables obtained in the analysis we computed their correlations (canonical loadings) with the original ones. Canonical correlations resulted in three canonical variables representing significant relationships between BAT and GBM data. The results of canonical correlation are summarized in Figs 5 and 6 for the BAT and Figs 7 and 8 for the GBM variables.

The strongest (*U,V*) pair (*U1,V1*) dominated by the fluences in both of the *Swift* and *Fermi* data. Since T_{90} and peak flux are correlating with fluence they also have strong correlations with the (*U1,V1*) pair.

Both of them strongly correlate with the pair (*U*2, *V*2). Since the canonical variables are perpendicular to each other, this does not result from a correlation with fluence, but from a direct relationship between BAT and GBM duration and peak flux.

The third (*U*3, *V*3) canonical variables show a weak but significant relationship between the BAT and the GBM durations. As Figs 5, 6, 7, 8, and 9 demonstrates both BAT and GBM durations has some but decreasing level of correlations with all the canonical variables.

The GBM bursts average peak energy is around 200 keV which is outside the sensitivity range of BAT (Pe'er 2015). Therefore, a significant fraction of photons detected and used in GBM durations is not detected by BAT may causing a non-linear relationship between BAT and GBM durations. Canonical correlation is a linear theory and therefore requires a system of more orthogonal vector for accounting non-linear relationships.

4 CLASSIFICATION OF *SWIFT* AND *FERMI* GRBS

According to Fig. 10, the duration of bursts detected jointly by *Fermi* and *Swift* is systematically longer based on *Fermi* measurements for

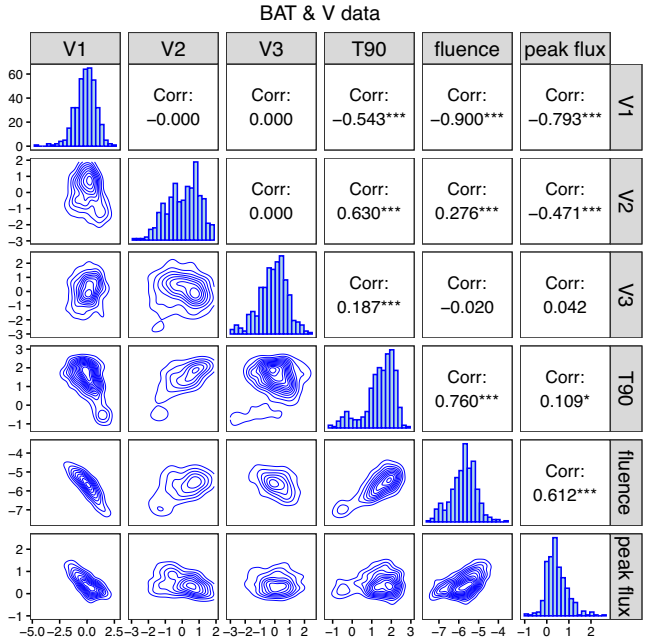

Figure 6. Matrix plot of BAT data and the canonical variables obtained from GBM (*V1*, *V2*, *V3*). Lower panel shows 2D densities the upper one the correlations between the variables. The significance level of the correlation indicated with stars at the right side of the numbers. Seemingly, the first (the strongest) canonical variable (*V1*) has the tightest correlation with fluence.

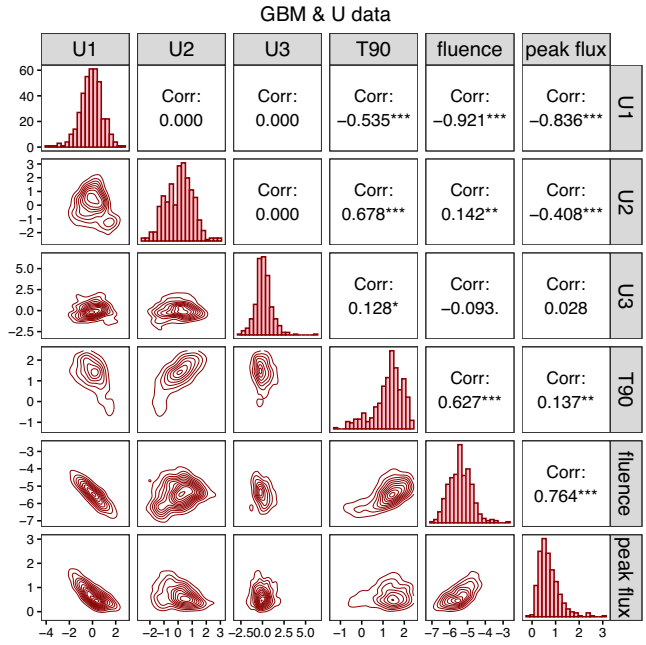

Figure 7. Matrix plot of GBM data and the canonical variables obtained from BAT (*U1,U2,U3*). Lower triangle panels show 2D densities the upper triangle ones the correlations between the variables. The significance level of the correlation indicated with stars at the right side of the numbers. Seemingly the first, strongest canonical variable (*U1*) has the tightest correlation with fluence.

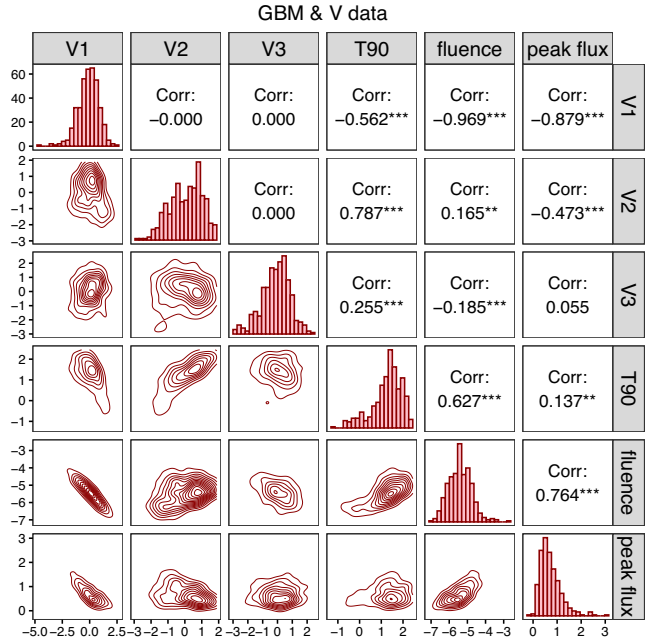

Figure 8. Matrix plot of GBM data and the canonical variables obtained from GBM (*V1,V2,V3*). Lower panel shows 2D densities the upper one the correlations between the variables. The significance level of the correlation indicated with stars at the right side of the numbers, Seemingly the first, the strongest, canonical variable (*V1*) has the tightest correlation with fluence.

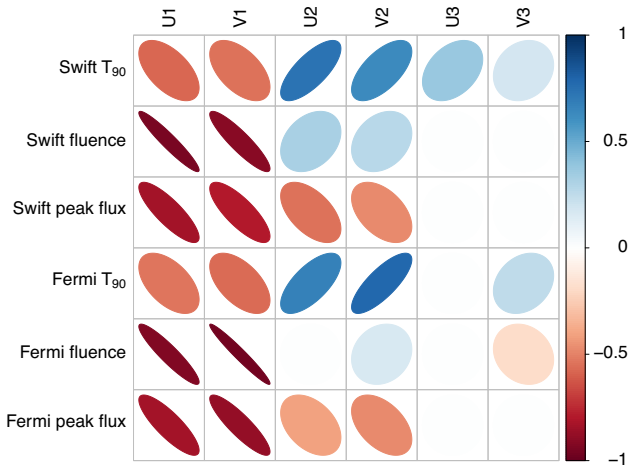

Figure 9. Coloured cross-correlation between the BAT and GBM data with the significant canonical variables. The size and colour of the circles indicate the strength of correlation. Correlations are indicated by the direction of tilt, positive marked with right-tilted blue, negative with left-tilted red ellipses. Correlations not reaching 3σ significance are left blank. The strongest canonical variable pair (*U1,V1*) has the tightest relation to fluence for both BAT and GBM.

the short GRBs, but the opposite is true for the long ones. If the durations obtained from the measurements of the two satellites were the same, the distribution in Fig. 2 could be fitted with a line with a slope of 1. However, the slope of the line that fits the points best is 0.75 ± 0.02.

We also mentioned in the introduction that burst triggering procedure and the spectral range of detection are different for the two satellites. Since the two satellites see the same burst, the actual

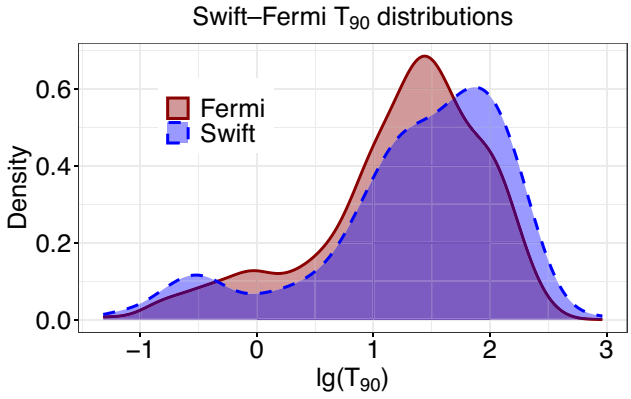

Figure 10. Distribution of T_{90} duration measured by *Fermi* (solid red line) an *Swift* (dashed blue line) satellites. The durations measured by *Fermi* are more concentrated at medium values, while those measured by *Swift* are more concentrated at short and long values, respectively.

physical duration of the phenomenon must be the same. However, changes in the physical parameters of the outburst as a function of time occur differently due to the different technical design of BAT and GBM. (see Lien et al. 2016; von Kienlin et al. 2020, to determine the duration of bursts for BAT).

Short bursts are generally harder, so they trigger GBM earlier and stay longer above detection level. For the long ones, since they are softer, it's just the opposite, in particular at the last stage of their spectral evolution. This is reflected in the deviation of points from $y = x$ line seen in Fig. 2 displaying the duration of the jointly observed bursts.

4.1 Fitting T_{90} distributions of GRBs jointly detected by *Fermi* and *Swift*

To perform fitting the T_{90} distribution by means of superposing lognormal distributions we used *Mclust()* procedure in the *mclust* library of **R**. Using these lognormal mixture models the procedure computes Bayesian information criterion (BIC) values starting with $g = 1$ Gaussian component and proceeds to a given higher g value. This BIC value is formally defined as $BIC = k \cdot ln(n) - 2 \cdot ln(L)$, where k is the number of parameters estimated by the model, n the number of data points, and L the maximized value of the likelihood function. The optimum k number of parameters is obtained at the highest BIC value. The result is given in Fig. 11 for *Swift* (blue colour) and *Fermi* (red colour), respectively.

BIC variance was calculated with jackknife cross-validation technique using *jackknife()* in the *bootstrap* library of **R** (Efron & Tibshirani 1993), and yielded a maximum variance of 1.97^2.

For determining the probabilities of the different number of lognormal components we applied likelihood ratio test statistics with 100 000 bootstrap replications to obtain the probabilities of the different groups for both satellites (McLachlan & Basford 1988). These probabilities can be seen in Table 3. From the results we can infer that in the case of BAT to fit the data best *three* lognormal components are required with a confidence larger than 4σ. On the other hand, GBM data can also be fitted with *two* components with more than 4σ confidence, but with less than 3σ for *three* components.

We found that the number of its best-fitting distribution components was different for *Fermi* and *Swift* measurements, although in both cases the GRBs were the same. It is worth mentioning Salmon, Hanlon & Martin-Carrillo (2022) made a 2D clustering of *Swift*/BAT and Fermi/GBM Gamma-ray Bursts and also found two groups for GBM and three for BAT.

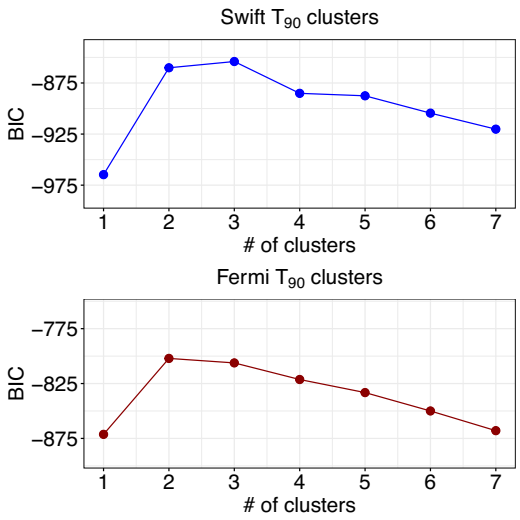

Figure 11. BIC values of the fitted multicomponent lognormal models. The maximum value of BIC for *Swift* (blue, top panel) is at three components, while for *Fermi* (red, bottom panel) it is two components, although both satellites measured the same GRBs. Even the largest deviation of BICs (± 1.97 at 4 clusters in *Swift* data) is smaller than the dots.

Table 3. The probability of the number of groups to which the data can be separated. The boldface numbers indicate significant improvements.

No. of groups	*Swift* BAT	*Fermi* GBM
	Probability	
$1 \Longrightarrow 2$	**<0.00001**	**<0.00001**
$2 \Longrightarrow 3$	**0.00006**	0.00685
$3 \Longrightarrow 4$	0.88545	0.32541

As we mentioned above (and can be seen in Fig. 10) *Swift* is more sensitive on the short and long parts of the T_{90} range, while *Fermi* in the middle. Since both distributions are given by the same GRBs, we have to conclude that the T_{90} distribution obtained from the observations cannot necessarily be inferred directly for the number of physical engine types operating in the background.

As we pointed out, the effect can be explained by considering the different energy sensitivity ranges used by *Fermi* and *Swift* satellites to calculate the physical parameters. As we mentioned, the *Fermi* parameters are calculated from the photons in the energy range of 10–1000 keV and that of *Swift* in the 15–150 keV range. Since bursts are initially harder and then gradually become softer during bursts (see e.g. Rácz & Hortobagyi 2018) *Fermi* may notice them earlier than *Swift*. Although, the 15–150 keV range is detected by both satellites, but here *Swift* is more sensitive. Therefore, bursts can be followed for a longer time period.

5 CONCLUSIONS

We examined how the technical properties of the *Swift* and *Fermi* satellites affect the observable properties of the GRBs they detect. In our study, we examined the data obtained from *Swift* BAT and *Fermi* GBM instruments. These data were duration, fluence, and peak flux for both satellites.

In order to identify GRBs detected jointly by *Swift* and *Fermi* we looked for coincidences in GRB angular position–trigger time

parameter space. For this purpose we used the *knn()* procedure available in *FNN* library of the **R** statistical package.

Based in these identifications we separated the 'couples' and 'widows' GRBs, the former were detected simultaneously by both satellites and the latter only by one of them. In case of the 'couples' the values of T_{90} are satisfactorily the same for the medium duration, while the data of the *Fermi* GBM are systematically higher in the case of the short ones and the data of the *Swift* BAT in the case of the long ones. For fluence and peak flux, the *Fermi* satellite measured a systematically larger value for the same GRB.

Using the LDA we compared the physical properties of 'couples' and 'widows' GRBs in BAT and GBM. For this purpose we utilized the *lda()* procedure available in the *MASS* library of **R** statistical package. LDA resulted a direction in the parameter space of observed variables where the difference between the 'couples' and 'widows' group is the greatest. We obtained that fluence has the highest discriminant power in case of *Swift* and peak flux in *Fermi*.

Using canonical correlation we studied the strength of the relationship between GRB parameters measured by *Swift* and *Fermi*, respectively. This relationship is represented by three orthogonal canonical variable pairs. The strongest of these has the largest contribution from fluence for both *Swift* and *Fermi*.

We tested the hypothesis that the number of lognormal distributions used to fit GRBs to T_{90} distribution could be inferred for the physical mechanisms responsible for bursts. For this purpose, we compared the distributions of the T_{90} jointly detected by the two satellites in the *Swift* and *Fermi* data, separately. Since the GRBs used for this analysis are the same at both satellites one expect the same number of lognormal components necessary to fit the T_{90} distributions. In contrast, we obtained that the number of lognormal components required is *three* for *Swift*, while it is only *two* for *Fermi*. Since the GRBs used for the analysis were the same in both cases, we concluded that it is not possible to infer the number of physical mechanisms responsible for GRBs from the T_{90} distribution alone.

ACKNOWLEDGEMENTS

The authors would like to thank Jakub Řípa and Mariusz Tarnopolski for numerous discussions on GRBs, and the valuable comments and suggestions by the anonymous referee. We are indebted to Jakub Řípa for initiating the writing of this paper. The authors thank the Hungarian TKP2021-NVA-16 and OTKA K-146092 program for their support.

DATA AVAILABILITY

The data underlying this paper are available in Swift GRB table at https://swift.gsfc.nasa.gov/archive/grb_table/ and *Fermi* GBM Burst Catalogue at https://heasarc.gsfc.nasa.gov/W3Browse /fermi/fermigbrst.html. The **R** scripts used for this study can be found on GitHub (https://github.com/sanya008/fermi-swift-comp.git).

REFERENCES

Atwood W. B. et al., 2009, ApJ, 697, 1071
Bagoly Z., Szécsi D., Balázs L. G., Csabai I., Horváth I., Dobos L., Lichtenberger J., Tóth L. V., 2016, A&A, 593, L10
Balastegui A., Ruiz-Lapuente P., Canal R., 2001, MNRAS, 328, 283
Barthelmy S. D., Cline T. L., Butterworth P., Kippen R. M., Briggs M. S., Connaughton V., Pendleton G. N., 2000, in Kippen R. M., Mallozzi R. S., Fishman G. J., eds, AIP Conf. Ser. Vol. 526, Gamma-ray Bursts, 5th Huntsville Symposium. Am. Inst. Phys. , New York, p. 731
Barthelmy S. D. et al., 2005, Space Sci. Rev., 120, 143
Beygelzimer A., Kakadet S., Langford J., Arya S., Mount D., Li S., 2019, FNN: Fast Nearest Neighbor Search Algorithms and Applications. Available at: https://CRAN.R-project.org/package=FNN
Bhat P. N. et al., 2009, Meegan C., Meegan C. Gehrels N., Kouveliotou C., eds, AIP Conf. Proc. Vol. 1133, The Fermi Gamma-ray Burst Monitor Instrument . Am. Inst. Phys., New York, p. 34
Biltzinger B., Kunzweiler F., Greiner J., Toelge K., Burgess J. M., 2020, A&A, 640, A8
Bissaldi E. et al., 2009, Meegan C., Gehrels N., Kouveliotou C., eds, AIP Conf. Proc. Vol. 1133, Fermi GBM: Main Detector-Level Calibration Results. Am. Inst. Phys., New York, p. 37
Bombaci I., Datta B., 2000, ApJ, 530, L69
Borgonovo L., 2004, A&A, 418, 487
Burns E., Connaughton V., Zhang B.-B., Lien A., Briggs M. S., Goldstein A., Pelassa V., Troja E., 2016, ApJ, 818, 110
Burrows D. N. et al., 2000, in Flanagan K. A., Siegmund O. H., eds, Proc. SPIE Conf. Ser. Vol. 4140, X-Ray and Gamma-Ray Instrumentation for Astronomy XI. SPIE, Bellingham, p. 64
Chattopadhyay T., Misra R., Chattopadhyay A. K., Naskar M., 2007, ApJ, 667, 1017
Citterio O. et al., 1996, in Hoover R. B., Walker A. B., eds, Proc. SPIE Conf. Ser. Vol. 2805, Multilayer and Grazing Incidence X-Ray/EUV Optics III. SPIE, Bellingham, p. 56
Deng Q. et al., 2022, ApJ, 940, 5
Efron B., Tibshirani R., 1993, An Introduction to the Bootstrap. Springer, Berlin, Germany
Fischer R. A., 1936, Ann. Eugenics, 7, 179
Fishman G. J., Meegan C. A., Wilson R. B., Paciesas W. S., Pendleton G. N., 1992, in Shrader C. R., Gehrels N., Dennis B., eds, NASA Conference Publication. National Aeronautics and Space Administration, Washington, D.C., p.26
Fitzpatrick G., McBreen S., Connaughton V., Briggs M., 2012, in Takahashi T., Murray S. S., den Herder J.-W. A., eds, Proc. SPIE Conf. Ser. Vol. 8443, Space Telescopes and Instrumentation 2012: Ultraviolet to Gamma Ray. SPIE, Bellingham, p. 84433B
Fordham J. L. A., Bone D. A., Read P. D., Norton T. J., Charles P. A., 1989, MNRAS, 237, 513
Gehrels N. et al., 2004, ApJ, 611, 1005
Goldstein A. et al., 2012, ApJS, 199, 19
González I., Déjean S., 2021, CCA: Canonical Correlation Analysis. Available at: https://CRAN.R-project.org/package=CCA
Gruber D. et al., 2014, ApJS, 211, 12
Hakkila J., Haglin D. J., Pendleton G. N., Mallozzi R. S., Meegan C. A., Roiger R. J., 2000, ApJ, 538, 165
Hill J. E., Zugger M. E., Shoemaker J., Witherite M. E., Koch T. S., Chou L. L., Case T., Burrows D. N., 2000, in Flanagan K. A., Siegmund O. H., eds, Proc. SPIE Conf. Ser. Vol. 4140, X-Ray and Gamma-Ray Instrumentation for Astronomy XI. SPIE, Bellingham, p. 87
Holland A. D., Turner M. J., Abbey A. F., Pool P. J., 1996, in Siegmund O. H., Gummin M. A., eds, Proc. SPIE Conf. Ser. Vol. 2808, EUV, X-Ray, and Gamma-Ray Instrumentation for Astronomy VII. SPIE, Bellingham, p. 414
Horváth I., 1998, ApJ, 508, 757
Horváth I., 2002, A&A, 392, 791
Horváth I., Tóth B. G., 2016, Ap&SS, 361, 155
Horváth I., Mészáros A., Balázs L. G., Bagoly Z., 2004, Baltic Astron., 13, 217
Horváth I., Balázs L. G., Bagoly Z., Veres P., 2008, A&A, 489, L1
Horváth I., Bagoly Z., Balázs L. G., de Ugarte Postigo A., Veres P., Mészáros A., 2010, ApJ, 713, 552
Horváth I., Hakkila J., Bagoly Z., Tóth L. V., Rácz I. I., Pintér S., Tóth B. G., 2019, Ap&SS, 364, 105
Hotelling H., 1933, J. Educ. Psychol., 24, 498
Huang Y. F., Dai Z. G., Lu T., Cheng K. S., Wu X. F., 2003, ApJ, 594, 919
Huja D., Mészáros A., Řípa J., 2009, A&A, 504, 67
von Kienlin A. et al., 2020, ApJ, 893, 46
King A., Olsson E., Davies M. B., 2007, MNRAS, 374, L34

Klebesadel R. W., Strong I. B., Olson R. A., 1973, ApJ, 182, L85
Kouveliotou C., Meegan C. A., Fishman G. J., Bhat N. P., Briggs M. S., Koshut T. M., Paciesas W. S., Pendleton G. N., 1993, ApJ, 413, L101
Kumar P., Zhang B., 2015, Phys. Rep., 561, 1
Lien A. et al., 2016, ApJ, 829, 7
Martinez A. M., Kak A. C., 2001, IEEE Trans. Pattern Anal. Mach. Intell., 23, 228
Mason K. O. et al., 2001, A&A, 365, L36
McLachlan G. J., 2004, Discriminant Analysis and Statistical Pattern Recognition. Wiley Interscience, New York City
McLachlan G. J., Basford K. E., 1988, Mixture Models: Inference and Applications to Clustering (Statistics: textbooks and monographs v.84). M. Dekker, New York
Meegan C. et al., 2009, ApJ, 702, 791
Menzel U., 2012, CCP: Significance Tests for Canonical Correlation Analysis (CCA). Available at: https://CRAN.R-project.org/package=CCP
Mészáros P., 2006, Rep. Prog. Phys., 69, 2259
Meszaros P., Rees M. J., 1993, ApJ, 405, 278
Mukherjee S., Feigelson E. D., Jogesh Babu G., Murtagh F., Fraley C., Raftery A., 1998, ApJ, 508, 314
Narayana Bhat P. et al., 2016, ApJS, 223, 28
Paciesas W. S. et al., 2012, ApJS, 199, 18
Pe'er A., 2015, Adv. Astron., 2015, 907321
Piran T., 2004, Rev. Mod. Phys., 76, 1143
R Core Team, 2017, R: A Language and Environment for Statistical Computing. R Foundation for Statistical Computing, Vienna, Austria. Available at: https://www.R-project.org
Rácz I. I., Hortobagyi A. J., 2018, Astron. Nachr., 339, 347
Racz I. I., Balázs L. G., Bagoly Z., Horvath I., Tóth L. V., 2018a, Astron. Nachr., 339, 352
Racz I. I., Balázs L. G., Horvath I., Tóth L. V., Bagoly Z., 2018b, MNRAS, 475, 306
Ripley B. D., 1996, Pattern Recognition and Neural Networks. Cambridge Univ. Press, Cambridge
Roming P. W. A. et al., 2005, Space Sci. Rev., 120, 95
Rueda J. A. et al., 2018a, EPJ Web Conf., 168, 01006
Rueda J. A. et al., 2018b, J. Cosmol. Astropart. Phys., 2018, 006
Salmon L., Hanlon L., Martin-Carrillo A., 2022, Galaxies, 10, 77
Short A. D., Keay A., Turner M. J., 1998, in Siegmund O. H., Gummin M. A., eds, Proc. SPIE Conf. Ser. Vol. 3445, EUV, X-Ray, and Gamma-Ray Instrumentation for Astronomy IX. SPIE, Bellingham, p. 13
Szécsi D., Bagoly Z., Kóbori J., Horváth I., Balázs L. G., 2013, A&A, 557, A8
Tarnopolski M., 2015, A&A, 581, A29
Tarnopolski M., 2016, MNRAS, 458, 2024
Tarnopolski M., 2019, ApJ, 870, 105
von Kienlin A. et al., 2014, ApJS, 211, 13
von Kienlin A. et al., 2020, ApJ, 893, 46
Venables W. N., Ripley B. D., 2002, Modern Applied Statistics with S, 4th edn. Springer, New York. Available at: http://www.stats.ox.ac.uk/pub/MASS4
Wells A. et al., 1992, in Hoover R. B., ed., Proc. SPIE Conf. Ser. Vol. 1546, Multilayer and Grazing Incidence X-Ray/EUV Optics. SPIE, Bellingham, p. 205
Wells A. A. et al., 1997, in Siegmund O. H., Gummin M. A., eds, Proc. SPIE Conf. Ser. Vol. 3114, EUV, X-Ray, and Gamma-Ray Instrumentation for Astronomy VIII. SPIE, Bellingham, p. 392
Yu H., Yang J., 2001, Pattern Recognit., 34, 2067
Zhang B., 2018, The Physics of Gamma-Ray Bursts. Cambridge Univ. Press, Cambridge
Zhang L., Luo J.-J., Huang Y.-F., Gong Y.-J., Wu S., 2022, MNRAS, 517, 5770
Zitouni H., Guessoum N., Azzam W. J., Mochkovitch R., 2015, Ap&SS, 357, 7

This paper has been typeset from a TEX/LATEX file prepared by the author.